

Spectropolarimetric follow-up of 8 rapidly rotating, X-ray bright FK Comae candidates

J. Sikora,^{1,*} J. Rowe,¹ S. B. Howell,² E. Mason,³ G. A. Wade⁴

¹*Department of Physics and Astronomy, Bishop's University, Sherbrooke, Québec, Canada, J1M 1Z7*

²*NASA Ames Research Center, Moffett Field, CA 94035, USA*

³*INAF-OATS, Via G.B. Tiepolo, 11, I-34143, Trieste, Italy*

⁴*Department of Physics and Space Science, Royal Military College of Canada, PO Box 17000 Kingston, Ontario, Canada, K7K 7B4*

Accepted 2020 May 12

ABSTRACT

Our understanding of the evolved, rapidly rotating, magnetically active, and apparently single FK Comae stars is significantly hindered by their extreme rarity: only two stars in addition to FK Com itself are currently considered to be members of this class. Recently, a sample of more than 20 candidate FK Comae type stars was identified within the context of the *Kepler-Swift* Active Galaxies and Stars (KSwAGS) survey. We present an analysis of high-resolution Stokes V observations obtained using ESPaDOnS@CFHT for 8 of these candidates. We found that none of these targets can be considered members of the FK Comae class based primarily on their inferred rotational velocities and on the detection of spectroscopic binary companions. However, 2 targets show evidence of magnetic activity and have anomalously high projected rotational velocities ($v \sin i$) relative to typical values associated with stars of similar evolutionary states. EPIC 210426551 has a $v \sin i = 209 \text{ km s}^{-1}$, an estimated mass of $1.07 M_{\odot}$, and, based in part on its derived metallicity of $[M/H] = -0.4$, it is either an evolved main sequence (MS) star or a pre-MS star. KIC 7732964 has a mass of $0.84 M_{\odot}$, lies near the base of the red giant branch, and exhibits a $v \sin i = 23 \text{ km s}^{-1}$. We find that these two objects have similar characteristics to FK Com (albeit less extreme) and that their rapid rotation may be inconsistent with that predicted for a single star evolutionary history. Additional observations are necessary in order to better constrain their evolutionary states and whether they have short-period binary companions.

Key words: Stars: activity, Stars: late-type, Stars: rotation, Stars: variables: general

1 INTRODUCTION

FK Comae type stars are amongst the most unusual non-degenerate stars that are currently known. These apparently single, red giant branch stars are defined largely by their high rotational velocities $\gtrsim 100 \text{ km s}^{-1}$ (Bopp & Rucinski 1981). FK Com itself has a projected rotational velocity of $v \sin i \approx 160 \text{ km s}^{-1}$ (Huenemoerder et al. 1993), which is particularly surprising considering that the majority of evolved stars have $v \sin i < 10 \text{ km s}^{-1}$ (e.g. de Medeiros et al. 1996; Cutispoto et al. 2002). FK Com also exhibits

enhanced magnetic activity as evidenced by the detection of (1) strong and variable $H\alpha$ and Ca II H and K emission (Herbig 1958; Ramsey et al. 1981), (2) highly energetic flares (Jetsu et al. 1991; Oliveira & Foing 1999), (3) a mean longitudinal magnetic field ranging from $\langle B_z \rangle \approx 60 - 272 \text{ G}$ (Korhonen et al. 2009), and (4) strong UV and X-ray emission (Bopp & Rucinski 1981; Ayres et al. 2016).

The FK Comae type stars are extremely rare since only two other members (ET Dra and HD 199178) have been discovered. A number of apparently single, evolved stars have been found with lower yet still anomalously high $v \sin i$ values of $10 - 80 \text{ km s}^{-1}$ (e.g. de Medeiros et al. 1996; Drake et al. 2002; Carlberg et al. 2011). As with FK Com, these rapid rotators appear to challenge our understanding of how the rotation rates of single stars evolve over time (e.g. Bouvier et al. 1997; Spada et al. 2011). One theory that has been proposed to explain these unexpectedly high rotation rates

* Based on observations obtained at the Canada-France-Hawaii Telescope (CFHT) which is operated by the National Research Council of Canada, the Institut National des Sciences de l'Univers of the Centre National de la Recherche Scientifique of France, and the University of Hawaii.

involves the transport of internal angular momentum from the star’s rapidly rotating core during the first dredge-up phase (Simon & Drake 1989; Fekel & Balachandran 1993); however, Privitera et al. (2016) argue that the acceleration of the star’s surface provided by such a scenario is largely insignificant. It has also been proposed that, as first outlined by Webbink (1976), the observed rapid rotation rates may be a byproduct of stellar merger events (e.g. Bopp & Rucinski 1981; Strassmeier et al. 1998; da Silva et al. 2015). In order to better understand how the rapid rotation rates of FK Comae type stars are produced, the small sample size likely needs to be increased.

As part of the *Kepler-Swift* Active Galaxies and Stars (KSwAGS) survey (Smith et al. 2015), simultaneous X-ray and UV observations were obtained for four modules of the *Kepler* Field of View (FOV) (~ 6 square degrees). These modules were surveyed in a series of tiled 2 ks observations using the *Swift* X-ray Telescope (XRT), which obtains both X-ray and UV images with an angular resolution of 18 arcseconds (Gehrels et al. 2004). Ninety-three X-ray sources were detected at signal-to-noise ratios (S/N) > 3 (i.e. 12 counts or 0.006 cts s^{-1} at the mean exposure time and background level of the snapshots).

The detected sources have X-ray to optical flux ratios exceeding 100 times the maximum value observed for the Sun. UV counterparts were also detected for 60 of the 93 X-ray sources. On the presumption that many of these sources may be FK Com candidates, Howell et al. (2016) carried out a study of 20 of the 60 X-ray and UV-bright sources with the primary goal of constraining these stars’ rotational velocities. Based on the available *Kepler* light curves and newly obtained medium-resolution optical spectra ($R \sim 7700 - 10000$), Howell et al. (2016) concluded that 18 of the 20 stars in their sample are apparently single, evolved, and rapidly rotating; their results are therefore consistent with the notion that a significant fraction of the 60 sources identified by the KSwAGS survey are similar in nature to FK Com and thus, they may be consistent with the predicted properties of stellar merger products.

The KSwAGS survey has continued to identify X-ray sources within several fields of the *K2* mission (Howell et al. 2014) based on newly obtained and archival measurements (K. Smith, private communication). These ongoing efforts have involved *Swift* XRT measurements, obtained using a similar observing strategy to that described by Smith et al. (2015), along with archival Chandra measurements and measurements obtained by the XMM-Slew Survey and the ROSAT All-Sky Survey. Low-resolution ($R \sim 500 - 4000$) optical follow-up spectra were obtained for those sources having $V \lesssim 17$ mag using the DeVeny spectrograph installed at the Discovery Channel Telescope at Lowell Observatory. From these spectra, no line measurements or luminosity class estimates were attempted; however, using standard MK spectral classification techniques (see e.g., Keenan & Morgan 1941; Garrison 1984), which make use of the shape and extent of the Balmer jump, the width and depth of broad molecular bands, and the general shape of the relative flux distribution, approximate spectral types were estimated. These rough classifications were not used to develop any of the stellar parameters used herein, but gave credence to the fact that the stars are FGK types and eyeball proof that the temperatures and derived luminosity classes re-

ported in the *Gaia* DR2 catalog (Andrae et al. 2018) are sensible.

In this study, we present new high-resolution Stokes V observations obtained using ESPaDOnS installed at the Canada France Hawaii Telescope (CFHT) for 8 stars that have been identified as FK Comae type candidates within the broader context of the KSwAGS survey. Three of these targets are discussed by Howell et al. (2016) while the remaining 5 targets were identified as bright X-ray sources in Fields 4 and 8 of the *K2* mission. The primary goals of our study are to (1) precisely measure each target’s $v \sin i$ value in order to identify or confirm their (presumed) rapid rotation rates, (2) search for evidence of binary companions (via radial velocity variations) that may provide an alternative explanation for the primary component’s rapid rotation (i.e. that the primary component has been spun-up by tidal interactions rather than by a stellar merger event), and (3) search for Zeeman signatures that are indicative of magnetic activity and organized magnetic fields. In Section 2, we discuss the new spectroscopic observations that were obtained along with the publicly available *Kepler* and *K2* light curves that are available for each target. The magnetic field and radial velocity measurements that we derive are presented in Section 3. In Section 4, we present our spectral modelling analysis from which $v \sin i$ and other fundamental parameters are derived. In Section 5, each target is compared with evolutionary model grids. Our analysis of the *Kepler* and *K2* light curves is presented in Section 6 in which we search for plausible signatures of rotational modulation. Finally, in Sections 7 and 8 we provide a discussion and a summary of our results.

2 OBSERVATIONS

The study presented here makes use of newly obtained spectropolarimetric measurements along with publicly available *Kepler* and *K2* light curves. Here we discuss those data sets.

2.1 ESPaDOnS Spectra

The 8 targets included in this study were observed using the high-resolution ($R \sim 65000$) échelle spectropolarimeter, ESPaDOnS, installed at CFHT. This instrument provides polarized (circular and linear) and unpolarized spectra spanning a wavelength range of approximately $3600 - 10000 \text{ \AA}$.

Circularly polarized (Stokes V) spectra were acquired using ESPaDOnS between Oct. 21, 2018 and June 11, 2019. The observing strategy involved obtaining 2 measurements separated in time by more than 1 week for each target. Four of the targets (EPIC 210355746, EPIC 210505125, EPIC 220533366, and KIC 4857678) were observed twice during this time span; these observations were separated in time by approximately 1 to 3 months. Due to scheduling and/or weather constraints, the remaining targets (EPIC 210384590, EPIC 210426551, KIC 6150124, and KIC 7732964) were only observed once. The observations have S/N s per CCD pixel ranging from as $\approx 20 - 120$ near a wavelength of $\lambda = 4000 \text{ \AA}$ to $\approx 100 - 590$ near $\lambda = 8000 \text{ \AA}$.

All of the observations were reduced using the Upena pipeline feeding the LIBRE-ESPRIT reduction software described by Donati et al. (1997). The pipeline automatically

Table 1. Spectral types, details of the obtained ESPaDOnS observations, derived radial velocities, and derived longitudinal magnetic field strengths. Columns 1 to 4 list each target’s identifier, spectral type, V magnitude, and the maximum S/N per pixel near 4000 Å and 8000 Å. Columns 5 to 7 list the HJDs, the v_r values of the primary and secondary (if a secondary component was detected) components. Columns 5 and 6 list the derived $\langle B_z \rangle$ values and the detection status (DD and ND corresponding to definite detection and no detection, respectively).

ID	Sp. Type	V (mag)	S/N (pxl ⁻¹)	Obs. HJD −2 458 000	$v_{r,A}$ (km s ⁻¹)	$v_{r,B}$ (km s ⁻¹)	$\langle B_z \rangle$ (G)	Detect. Status
(1)	(2)	(3)	(4)	(5)	(6)	(7)	(8)	(9)
EPIC 210355746		9.8	50/290	476.754	8.3 ± 0.5		−1.2 ± 6.2	ND
			50/300	564.719	8.5 ± 0.4		−2.8 ± 6.3	ND
EPIC 210384590	G0 ^a	9.0	70/400	476.778	23.7 ± 0.1		5.8 ± 1.9	DD
EPIC 210426551		10.3	40/280	477.779	10 ± 4		493 ± 335	ND
EPIC 210505125	G0 ^a	8.2	90/420	413.118	−40.2 ± 0.3	16.6 ± 0.5		ND
			80/380	441.887	7.8 ± 0.3	−33.1 ± 0.3		ND
EPIC 220533366	K0 ^a	8.8	50/470	413.826	−49.5 ± 0.7		−24.2 ± 3.5	DD
			30/410	475.772	−20.4 ± 0.6		−21.9 ± 3.5	DD
KIC 4857678	F3V ^b , F2-5III ^c	7.0	120/480	413.782	−22 ± 1		−58 ± 68	ND
			20/100	441.738	−22 ± 2		243 ± 327	ND
KIC 6150124	K0 ^a , G0-9III ^c	7.4	80/590	413.793	10.6 ± 0.2		1.0 ± 1.0	ND
KIC 7732964	G6-7IV-III ^c	11.1	30/210	645.828	−18.4 ± 0.9		−9.4 ± 10.0	DD [†]

^a Cannon & Pickering (1993), ^b Frasca et al. (2016), ^c Howell et al. (2016), [†]Signal also detected in diagnostic null.

applies wavelength corrections to account for the earth’s rotation and orbital motion and is capable of automatically normalizing the observations. We opted to manually normalize the spectra by fitting a polynomial (typically of order 1 or 2) to the continuum of each (unnormalized) spectral order. In Table 1, we list each target’s V magnitude, spectral type reported in the literature (if available), along with the exposure times, dates, and maximum S/Ns of the obtained observations.

2.2 Kepler and K2 Light Curves

Three of the 8 targets in our sample are located in the original *Kepler* FOV and 5 are located in Fields 4 and 8 of the *K2* mission. Optical light curves obtained with the *Kepler* spacecraft are publicly available for all of our targets. These light curves were downloaded from the Mikulski Archive for Space Telescopes (MAST)¹. All of the light curves have a cadence of 30 min. The *K2* light curves span a time period of ≈ 2.5 months (EPIC 210355746, EPIC 210384590, EPIC 210426551, EPIC 210505125, and EPIC 220533366) while the 3 *Kepler* light curves span either 2.4 yrs (KIC 4857678) or 4 yrs (KIC 6150124 and KIC 7732964).

We used the “presearch data condition simple aperture photometry” (PDC_SAP) light curves, which have been processed in such a way as to remove systematic errors including outliers, systematic trends, and instrumental signals (Smith et al. 2012). We carried out additional post-processing consisting of outlier removal and basic detrending in which a first order polynomial was fit to the full light curve and the flux measurements divided by the resulting fit.

3 LEAST-SQUARES DECONVOLUTION PROFILES

We generated Least-Squares Deconvolution (LSD) profiles (Donati et al. 1997; Kochukhov et al. 2010) for each of the measurements obtained using ESPaDOnS. LSD is a cross-correlation technique that combines a large number of similarly-shaped spectral lines in order to produce a pseudo line profile with a significantly higher S/N. We used the resulting Stokes I and V LSD profiles to (i) derive the radial velocities of all stellar components visible in the spectra and (ii) identify circularly polarized Zeeman signatures and derive the associated mean longitudinal field strengths ($\langle B_z \rangle$).

The LSD technique requires a line mask consisting of the wavelengths and relative depths of spectral lines that are expected to be found in the observed spectra based primarily on the star’s effective temperature (T_{eff}) and surface gravity ($\log g$). These masks were constructed using line lists generated by the ‘Extract Stellar’ tool provided by the Vienna Atomic Line Database (VALD) (Ryabchikova et al. 2015). The specified T_{eff} values were taken from the *Gaia* DR2 catalog (Andrae et al. 2018) and we adopted $\log g$ values of 3.0 or 4.0 (cgs) based on each star’s position in the Hertzsprung-Russell Diagram (presented in Sect. 5). All lines with wavelengths within the broad wings of the Balmer lines (i.e. within approximately 30 Å of the central Balmer line wavelength) were removed from the line masks along with the Balmer lines themselves and those lines that were found to be contaminated with tellurics. The Stokes I , Stokes V , and the two diagnostic null² (N_1 and N_2) LSD profiles were then computed using the normalized spectra and the generated line masks. In Fig. 1, we show all of the Stokes I and V LSD profiles associated with the stars in our sample.

² The diagnostic null fluxes obtained during each measurement are used to identify polarized signals that may be instrumental in origin (e.g. Donati et al. 1997).

¹ <https://archive.stsci.edu>

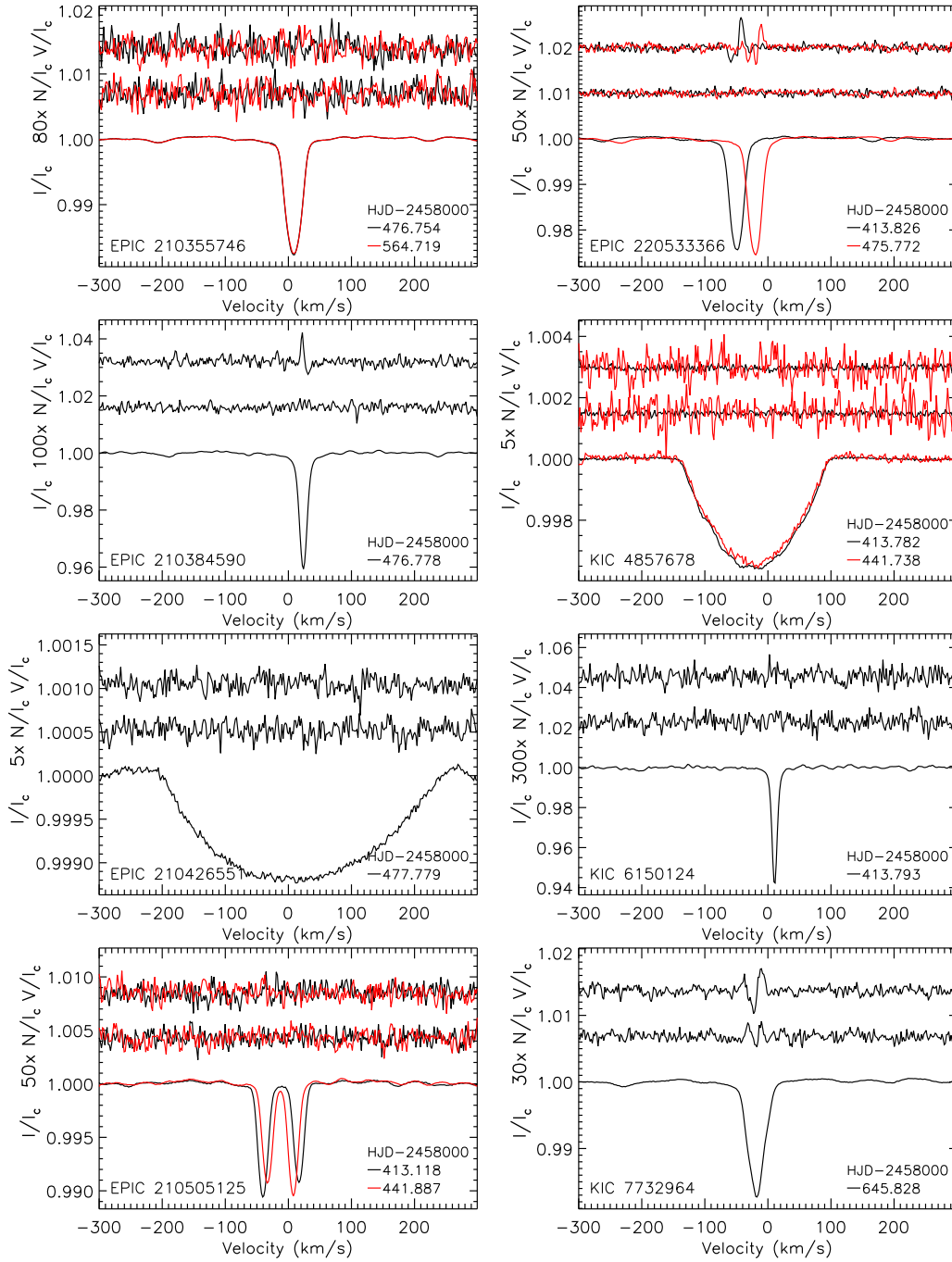


Figure 1. LSD pseudo-line profiles derived from the ESPaDOnS observations of the 8 targets included in this study. In each panel, the normalized Stokes V and I profiles are plotted (V/I_c and I/I_c ; top and bottom, respectively) along with the diagnostic null (N/I_c ; middle). Note that V/I_c and I/I_c have been shifted vertically and scaled for visual clarity. The appearance of positive and negative lobes in V/I_c correspond to circularly polarized Zeeman signatures produced by magnetic fields that are visible at the star’s surface. Similar features appearing in the diagnostic null (e.g. KIC 7732964) indicate that the detected Zeeman signatures may be instrumental in origin. Spectroscopic binary companions are clearly detected in I/I_c based on radial velocity variations (EPIC 220533366) and/or the presence of multiple components (EPIC 210505125).

3.1 Radial velocities and binarity

Based on the computed LSD profiles, only one target (EPIC 210505125) was found to consist of more than one spectral component. EPIC 210505125 exhibits two components that are similar both in terms of the widths and depths of their Stokes I profiles. Clear radial velocity shifts are

apparent between the two observations of EPIC 220533366 suggesting that it consists of at least one additional dimmer (relative to the primary component) companion.

We derived the radial velocities (v_r) associated with all of the stellar components that were detected by fitting Gaussian functions to the Stokes I profiles. Uncertainties

in the derived v_r values were estimated by bootstrapping the residuals in order to generate 500 bootstrapped data sets (see Sikora et al., submitted). We note that, in general, the Gaussian fits to the Stokes I profiles are of reasonably high quality. The largest residuals are associated with KIC 7732964, which exhibits moderate asymmetries; the four Stokes I sub-exposures used to obtain the Stokes V measurement reveal variability that affects the entire profile over a time period of 37 min, which suggests that the asymmetries in the averaged Stokes I profile is produced by pulsations. The resulting v_r values and their 3σ uncertainties derived for all of the targets in our sample are listed in Table 1.

3.2 Longitudinal magnetic field

In Fig. 1, clear circularly polarized Zeeman signatures, which are manifest as positive and negative lobes (i.e. systematic deviations from zero) in the Stokes V pseudo-line profiles, are detected for 3 of the 8 targets (EPIC 210384590, EPIC 220533366, and KIC 7732964). In the case of KIC 7732964, however, the same characteristic signal is visible in one of the two diagnostic null LSD profiles. This suggests that the detected Zeeman signature may not be intrinsic to the star but rather an observational artifact. Additional observations are required to confirm the presence of a detectable magnetic field at the star's surface.

We measured $\langle B_z \rangle$ from each of the observations using the computed Stokes I and V profiles using Eqn. 1 of Wade et al. (2000). We used mean wavelengths (≈ 480 nm) and mean Landé factors (≈ 1.2) that were calculated from the line masks discussed above in Sect. 3. Integration ranges were adopted such that they span the width of the Stokes I profiles (e.g. for EPIC 220533366, we used a width of 45 km s^{-1} ; for EPIC 210426551, we used a width of 383 km s^{-1}). In Table 1, we list the derived $\langle B_z \rangle$ measurements, their associated uncertainties, and the Zeeman signature detection probability (no detection or definite detection as specified by Donati et al. 1997).

4 SPECTRAL MODELLING

The high-resolution spectra obtained for this study can be used to constrain various fundamental parameters associated with the sample stars including T_{eff} , $\log g$, metallicity ($[M/H]$), the projected rotational velocity ($v \sin i$), the microturbulence (ξ), along with individual chemical abundances. We carried out a spectroscopic modelling analysis based largely on that described by Sikora et al. (submitted). This involved using the Grid Search in Stellar Parameters (GSSP) code published by Tkachenko (2015). The GSSP code generates grids of synthetic spectra computed from LLMODELS atmospheric models (Shulyak et al. 2004). The grids can be defined such that they span various ranges of the input parameters with associated grid resolutions.

Three regions within wavelengths of 7445 and 8825 Å and spanning approximately 100 Å in width were selected to be modelled. The selected regions are free from tellurics and the density of spectral lines is lower than that of the shorter wavelength regions contained within the ESPaDOnS spectra thereby reducing line blends. The modelling that was

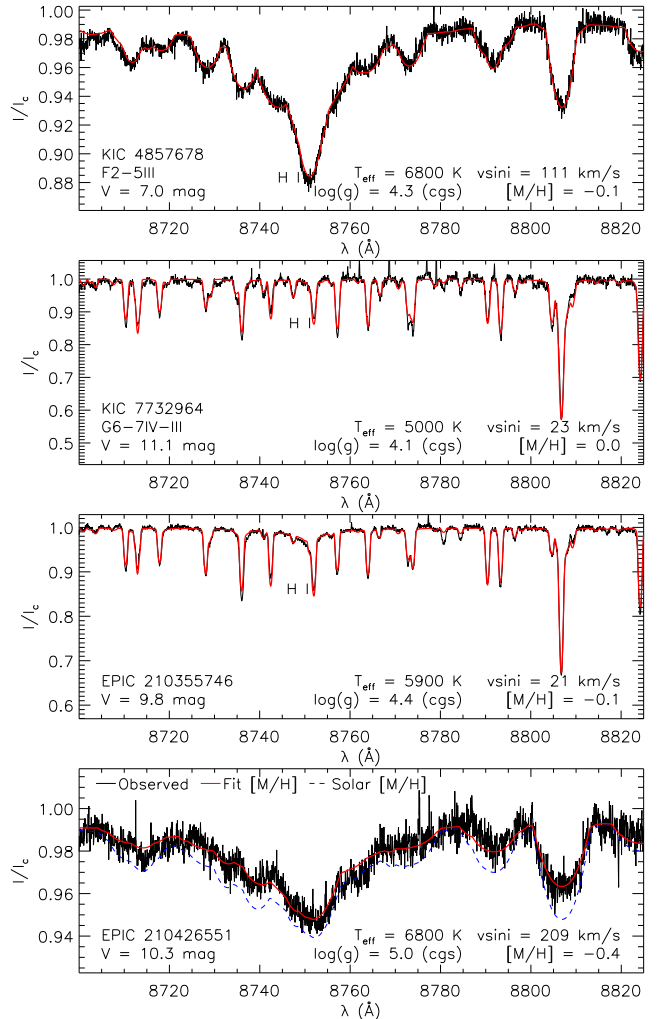


Figure 2. Examples of the fits to the 8700 – 8825 Å regions, which were used to derive T_{eff} , $\log g$, $[M/H]$, $v \sin i$, and ξ . The Paschen line (H I $\lambda 8750$) centered in these regions is labeled. The black curve corresponds to the observed spectra and the solid red curve corresponds to the best-fitting model. For EPIC 210426551, we also plot the model generated using the same fitting parameters but with a solar metallicity ($[M/H]=0$) (dashed blue).

carried out in order to derive T_{eff} , $\log g$, $[M/H]$, $v \sin i$, and ξ proceeded using two sets of grid parameters: wide, low-resolution grids were used in the first iteration and narrower, higher-resolution grids were used in the second iteration. The high-resolution grids were used to derive the best-fitting parameters while the χ^2 distributions associated with the low-resolution grids were used to estimate 1σ uncertainties for each parameter. The initial parameter grids were defined using the *Gaia* DR2 T_{eff} values, a $\log g$ of 3 (cgs), a solar metallicity (Asplund et al. 2009), a ξ of 2 km s^{-1} , and $v \sin i$ values that were estimated by eye. This procedure is similar to that employed by Sikora et al. (submitted). Ultimately, we found that the 8700 – 8825 Å region, which contains the Paschen line corresponding to the $n = 12$ to $n = 3$ transition (H I $\lambda 8750$), was more sensitive to changes in T_{eff} and $\log g$ compared to the 7450 – 7550 Å and 7710 – 7810 Å regions and yielded the highest-quality fits; therefore, the best-fitting parameters and their associated uncertainties were taken only from the fits to the 8700 – 8825 Å regions.

Table 2. Fundamental parameters derived from the spectral modelling analysis. Columns 1 and 2 list each target’s ID and T_{eff} values taken from the *Gaia* DR2 (Andrae et al. 2018). Columns 3 to 7 list the derived T_{eff} , $\log g$, ξ , $v \sin i$, and [M/H] values. All of the uncertainties associated with the derived parameters correspond to 1σ .

ID	$T_{\text{eff}}^{\text{GDR2}}$ (K)	T_{eff} (K)	$\log g$ (cgs)	ξ (km s^{-1})	$v \sin i$ (km s^{-1})	[M/H]
(1)	(2)	(3)	(4)	(5)	(6)	(7)
EPIC 210355746	5726^{+209}_{-152}	5900^{+160}_{-140}	4.4 ± 0.2	$1.0^{+0.6}_{-0.3}$	21 ± 1	-0.1 ± 0.1
EPIC 210384590	5581^{+119}_{-52}	5500^{+170}_{-120}	$4.4^{+0.3}_{-0.2}$	$1.5^{+0.2}_{-0.6}$	9 ± 1	0.0 ± 0.1
EPIC 210426551	5802^{+765}_{-179}	6800^{+100}_{-290}	> 4.6	< 1.7	209 ± 13	-0.4 ± 0.1
EPIC 220533366	4637^{+131}_{-105}	4700^{+110}_{-70}	$3.2^{+0.3}_{-0.2}$	$1.5^{+0.2}_{-0.3}$	17 ± 1	0.0 ± 0.1
KIC 4857678	6668^{+106}_{-150}	6800^{+130}_{-170}	$4.3^{+0.1}_{-0.3}$	< 1.2	111^{+6}_{-1}	-0.1 ± 0.1
KIC 6150124	5055^{+56}_{-62}	5000^{+240}_{-40}	$3.0^{+0.5}_{-0.4}$	$1.0^{+0.6}_{-0.1}$	4 ± 1	-0.2 ± 0.1
KIC 7732964	5000^{+114}_{-75}	5000^{+130}_{-200}	4.1 ± 0.4	$1.5^{+0.5}_{-0.6}$	23^{+1}_{-2}	0.0 ± 0.1

We roughly evaluated the sensitivity of the 8700 – 8825 Å region to changes in $\log g$ by using model spectra to estimate the maximum value of $\partial(I/I_c)/\partial(\log g)$. For each star, we generated a grid of models spanning a range of $\log g$ in increments of 0.5 while all other parameters were fixed at the best-fitting values. We found that for the 8700 – 8825 Å region, $\partial(I/I_c)/\partial(\log g)|_{\text{max}} \sim 0.02 - 0.1$; for comparison, we also computed $\partial(I/I_c)/\partial(\log g)|_{\text{max}}$ for a region centered on H α (6530 – 6590 Å), which yielded comparable values. Therefore, we conclude that the adopted 8700 – 8825 Å region is suitable for estimating $\log g$ to a degree that is acceptable within the scope of this study. We also note that the best-fitting T_{eff} values yielded by the fits to all three regions (7450 – 7550, 7710 – 7810, and 8700 – 8825 Å) are in agreement within 500 K.

Essentially all of the fitting parameters that were derived from the 8700 – 8825 Å regions were reasonably well constrained; however, the $v \sin i$ value of EPIC 210426551 exhibited large 1σ uncertainties $\gtrsim 30$ per cent likely as a result of the high $v \sin i \gtrsim 150 \text{ km s}^{-1}$ and the relatively low S/N ~ 280 (compared to the other spectra obtained for this study). In this case, we constrained $v \sin i$ by fitting several (apparently) unblended Fe and Mg lines within 7445 – 8825 Å using the procedure described above. We adopted a $v \sin i$ value and associated uncertainty by taking the average and standard deviation of the resulting distribution. The values and the uncertainties of T_{eff} , $\log g$, [M/H], and ξ were then derived using the same method that was applied to the other stars while fixing $v \sin i$.

The $v \sin i$ values associated with the two components in the SB2 system, EPIC 210505125, were estimated using the Fast Fourier Transform method (e.g. Gray 2005; Simón-Díaz et al. 2006). This was carried out using various metal lines (e.g. Fe I, Mn I, Si I, and Cr I) located within the three ≈ 100 Å regions noted above. Each spectral component’s adopted $v \sin i$ value and its uncertainty were taken to be the mean and standard deviation, respectively, of the resulting distribution. We obtained approximately equal values for the ‘A’ and ‘B’ components (as labeled in Table 1) of 12.8 ± 1.8 and $11.7 \pm 2.2 \text{ km s}^{-1}$, respectively.

In Fig. 2, we show several examples of the fits to the 8700 – 8825 Å regions. Additional figures comparing the

best-fitting model spectra (i.e. the model spectra generated using the adopted fitting parameters) with the observed spectra for three selected spectral windows (4960 – 5050 Å, 7710 – 7810 Å, and 8700 – 8825 Å) are shown in Figures 6 to 12 in the online version of this paper. In Table 2, we list the fundamental parameters (T_{eff} , $\log g$, [M/H], $v \sin i$, and ξ) derived from the spectra. The table also lists the T_{eff} values found in the *Gaia* DR2 catalog ($T_{\text{eff}}^{\text{GDR2}}$) for comparison; we find that both the derived T_{eff} values and the $T_{\text{eff}}^{\text{GDR2}}$ values are in agreement within their respective 1σ uncertainties for all of the stars. Note that the spectral modelling analysis was not carried out for the SB2 system EPIC 210505125.

5 HERTZSPRUNG-RUSSELL DIAGRAM

As noted in Sect. 4, the T_{eff} values available in the *Gaia* DR2 catalog (Andrae et al. 2018) are generally in agreement with the values derived from the spectral modelling analysis. However, in the case of EPIC 210426551, the difference between these two values ($\approx 1000\text{K}$) is significant. Spectroscopically-derived T_{eff} values are generally more accurate than those derived using photometric calibrations (particularly for stars with $T_{\text{eff}} \gtrsim 7000\text{K}$, e.g. Molenda-Zakowicz et al. 2010; Brown et al. 2011); therefore, we opted to place our sample of stars on the Hertzsprung-Russell diagram (HRD) using the T_{eff} values derived from the spectra in conjunction with luminosities derived using the distance estimates that have been inferred from the *Gaia* DR2 parallax measurements (Gaia Collaboration et al. 2018).

We derived radii (R) and luminosities (L) for the 7 stars with spectroscopically-derived T_{eff} values by fitting synthetic spectral energy distributions (SEDs) to published photometric measurements. This was carried out using a procedure similar to that discussed by Sikora et al. (submitted). Measurements obtained using various photometric filters were compiled including Johnson B_V , Tycho $B_T V_T$ (ESA 1997), Strömgren $ubvy$ (Hauck & Mermilliod 1998), *Gaia* DR2 $GG_{BP}GRP$ (Gaia Collaboration et al. 2018), 2MASS JHK (Cohen et al. 2003), and WISE $W_1 W_2 W_3 W_4$ (Wright et al. 2010). We used reddening parameters ($E[B - V]$) published by Gontcharov & Mosenkov (2017) and distances were taken from the catalog published

Table 3. Various parameters associated with the HRD. Columns 2 to 4 list the distance reported by Bailer-Jones et al. (2018) based on *Gaia* DR2 parallax measurements and the derived or adopted R and $\log L$ values. Columns 4 to 7 list the masses (M), ages (t_{age}), fractional MS ages (τ), and critical rotational velocities (v_{crit}).

ID	d (pc)	R (R_{\odot})	$\log(L/L_{\odot})$	M (M_{\odot})	t_{age} (Gyrs)	τ	v_{crit} (km s^{-1})
(1)	(2)	(3)	(4)	(5)	(6)	(7)	(8)
EPIC 210355746	125.2 ± 0.7	1.18 ± 0.04	0.18 ± 0.07	$0.97^{+0.07}_{-0.04}$	$9.99^{+0.08}_{-0.24}$	$1.10^{+0.09}_{-0.30}$	307^{+29}_{-11}
EPIC 210384590	61.2 ± 0.2	0.94 ± 0.04	-0.14 ± 0.08	$0.86^{+0.08}_{-0.03}$	$10.1^{+0.2}_{-0.4}$	$0.9^{+0.2}_{-0.4}$	336 ± 19
EPIC 210426551	184 ± 2	1.26 ± 0.09	0.5 ± 0.1	$1.05^{+0.09}_{-0.05}$	9.6 ± 0.3	$1.1^{+0.1}_{-0.4}$	306^{+37}_{-16}
EPIC 210505125	77.0 ± 0.3	$1.06^{+0.06}_{-0.07}$	$0.134 \pm 0.002^{\dagger}$	$1.04^{+0.08}_{-0.07}$	$9.8^{+0.2}_{-0.5}$	$0.8^{+0.2}_{-0.4}$	343 ± 16
EPIC 220533366	254 ± 4	7.1 ± 0.4	1.34 ± 0.08	$1.2^{+0.4}_{-0.1}$	$9.4^{+0.4}_{-0.2}$	1.3 ± 0.2	154 ± 13
KIC 4857678	54.66 ± 0.08	1.36 ± 0.04	0.55 ± 0.06	$1.29^{+0.05}_{-0.07}$	$9.4^{+0.1}_{-0.3}$	$0.7^{+0.2}_{-0.3}$	331 ± 18
KIC 6150124	257 ± 2	12.2 ± 0.5	1.92 ± 0.09	2.2 ± 0.3	$8.77^{+0.06}_{-0.24}$	1.033 ± 0.009	182^{+18}_{-34}
KIC 7732964	182 ± 4	1.43 ± 0.08	0.1 ± 0.1	$0.77^{+0.09}_{-0.03}$	10.3 ± 0.1	$1.26^{+0.03}_{-0.04}$	263 ± 12

[†]Taken from Andrae et al. (2018) and adjusted to account for binarity ($L \rightarrow L/2$ and $R \rightarrow R/\sqrt{2}$).

by Bailer-Jones et al. (2018) based on *Gaia* DR2 parallax measurements. Synthetic SEDs published by Castelli & Kurucz (2003) were fit to the photometric measurements by fixing T_{eff} , $\log g$, and $[M/H]$ to the best-fitting values listed in Table 2 while allowing R to vary. The uncertainty in R was estimated using a bootstrapping procedure and subsequently including the uncertainty in the distances, as described by Sikora et al. (submitted). Finally, luminosities were derived using the T_{eff} and R values through the Stefan-Boltzmann relation.

EPIC 210505125 is an SB2 system that is unresolved within the *Gaia* DR2 catalog (Gaia Collaboration et al. 2018). The two stars have similar spectral types (see Fig. 1) and therefore their reported T_{eff} values are unlikely to be significantly altered from their true values. The luminosities of the individual stars, on the other hand, are likely overestimated by approximately a factor of 2. We adopt the effective temperature and half of the luminosity ($L/2$) reported within the *Gaia* DR2 catalog (Andrae et al. 2018).

In Fig. 3, we show the HRD containing the 8 targets in our sample colour-coded by their derived $v \sin i$ values. We also plot the grid of solar-metallicity, rotating ($v/v_{\text{crit}} = 0.4$) evolutionary model tracks published by Ekström et al. (2012). The non-rotating $Z = 0.002$ and $Z = 0.014$ grids of evolutionary models published by Georgy et al. (2013) and Ekström et al. (2012) along with the non-rotating $Z = [0.006, 0.04]$ grids published by Mowlavi et al. (2012) were linearly interpolated in order to derive each star’s mass and age (i.e. evolutionary state) based on the adopted T_{eff} , L , and $[M/H]$ values. For EPIC 210505125, which is located at a distance of 77.0 ± 0.3 pc, we assume $[M/H] = 0.0 \pm 0.2$ where the uncertainty corresponds to the standard deviation of the solar neighbourhood’s $[M/H]$ distribution reported by Casagrande et al. (2011).

Uncertainties in the parameters derived from the evolutionary models were estimated using the Monte Carlo method discussed by Sikora et al. (2019a), which is based on that used by Shultz et al. (2019). This involves generating ~ 3000 T_{eff} , L , and $[M/H]$ points randomly sampled from distributions defined by the adopted values and their uncer-

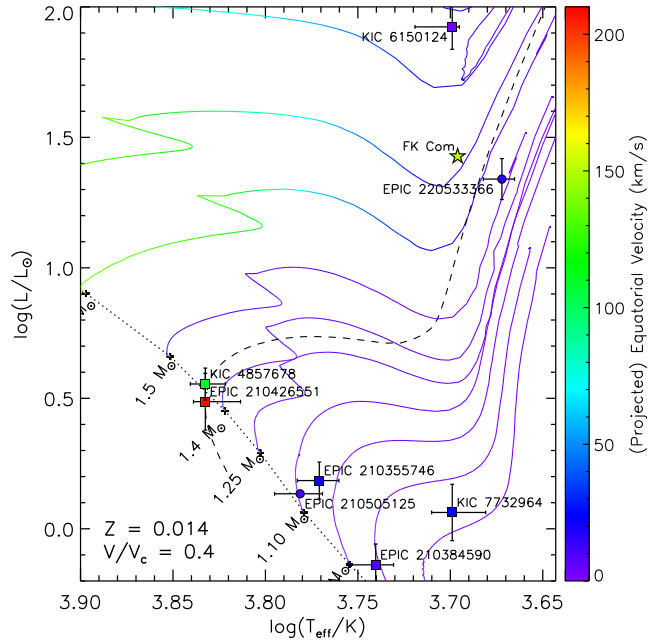


Figure 3. HRD associated with the targets observed for this study compared with the solar metallicity ($Z = 0.014$), rotating models ($v_{\text{eq}}/v_{\text{c}} = 0.4$) generated by Ekström et al. (2012) (solid lines); the dotted black line indicates the ZAMS. Circle symbols correspond to spectroscopic binaries while square symbols correspond to those stars for which no spectroscopic signatures of companions were detected. FK Com is plotted for reference based on its *Gaia* DR2 stellar parameters (Andrae et al. 2018). The colours of the square and circle symbols correspond to the $v \sin i$ values of those objects while the colours of the evolutionary tracks correspond to the associated equatorial velocities. We also plot the best-fitting non-rotating evolutionary track associated with EPIC 210426551, which corresponds to $M = 1.08 M_{\odot}$ and $Z = 0.006$ ($[M/H] = -0.4$) (dashed black).

tainties. For each of these points, relevant parameters are derived from the evolutionary grids (mass, age, etc.) and the resulting distributions are used to estimate 1σ uncertainties. Note that in several cases, the randomly sampled distribu-

Table 4. Parameters associated with or derived from the *Kepler* and *K2* light curves. Column 2 lists the minimum rotation period estimated using the v_{crit} values listed in Table 3. Column 3 lists the minimum rotation period estimated from the derived $v \sin i$ values. Column 4 lists the periods identified in the light curves that are most likely attributed to the star’s rotation and column 5 lists the equatorial velocity inferred from P_{phot} (under the assumption that $P_{\text{phot}} = P_{\text{rot}}$). Values listed in parentheses correspond to uncertainties in the last digit.

ID	$P_{\text{rot}}^{\text{min}}$	$P_{\text{rot}}^{\text{max}}$	P_{phot}	$v_{\text{eq}}^{\text{phot}}$
	(d)	(d)	(d)	(km s^{-1})
(1)	(2)	(3)	(4)	(5)
EPIC 210355746	0.18	3.1	2.929717(4)	20.5(6)
EPIC 210384590	0.14	6.0	5.152970(4)	9.22(4)
EPIC 210426551	0.20	0.35	0.346259240(3)	184(12)
EPIC 210505125	0.16	6.0	3.81298(1)	14.1(8)
EPIC 220533366	2.2	22.9	14.00744(1)	26(1)
KIC 4857678	0.20	0.641		
KIC 6150124	3.0	200	31.3698(1)	19.7(8)
KIC 7732964	0.26	3.7	2.4441471(1)	30(2)

tions contain $[M/H]$ values that fall outside of the model grid limits; therefore, in these cases the upper uncertainty in mass and lower uncertainty in age may be truncated. Furthermore, the models do not include the pre-MS, which also contributes to the truncation of the lower age uncertainty. In Table 3, we list the derived (and adopted) radii and luminosities along with the derived masses and ages for the 8 stars in our sample. We also report the fractional MS age (i.e. the age divided by the MS lifetime, τ) and the critical equatorial rotational velocity (v_{crit} , as defined in Eqn. 3.14 of Maeder & Meynet 2000).

Most of the stars in our sample that were included in the spectral modelling analysis (Sect. 4) were found to have metallicities approximately consistent with solar values (Asplund et al. 2009). The largest deviation from a solar metallicity is exhibited by EPIC 210426551 ($[M/H] = -0.4 \pm 0.1$, which is within 2.4σ of the average metallicity within the solar neighbourhood; Casagrande et al. 2011). Comparing the grids of evolutionary models, it is clear that adopting a lower metallicity will yield a lower inferred mass and imply that the star is more evolved. Therefore, in Fig. 3, we plot the best-fitting evolutionary track associated with EPIC 210426551 (i.e. the interpolated model that passes through the derived T_{eff} , L , and $[M/H]$ values).

6 LIGHT CURVES

The *Kepler* and *K2* light curves used in this study are shown in Fig. 4 along with their associated Lomb-Scargle (LS) periodograms (Lomb 1976; Scargle 1982). All of the light curves exhibit clear variability with amplitudes ranging from $\sim 0.1 - 100$ mmag. Multiple peaks with frequencies $\lesssim 10 \text{ d}^{-1}$ are apparent in each of the LS periodograms. While some of these signals correspond to oscillation frequencies (e.g. $f \approx 3.5 \text{ d}^{-1}$ in KIC 6150124, Yu et al. 2018), others may be associated with the presence of spots on the rotating star’s

surface and thus, they may correspond to the star’s rotation period (P_{rot}).

In order to identify potential rotational modulation signatures, we estimated lower and upper frequency limits based on (1) the $v \sin i$ values derived in Sect. 4 ($f_{\text{rot}}^{\text{min}} = 1/P_{\text{rot}}^{\text{max}} \equiv v \sin i / 2\pi R$) and (2) the v_{crit} values derived in Sect. 5 ($f_{\text{rot}}^{\text{max}} = 1/P_{\text{rot}}^{\text{min}} \equiv v_{\text{crit}} / 2\pi R$). These $P_{\text{rot}}^{\text{min}}$ and $P_{\text{rot}}^{\text{max}}$ values (listed in Table 4) are computed using the lower and upper bounds of each relevant parameter. For each of the 8 targets, we searched for those peaks with frequencies within the $f_{\text{rot}}^{\text{min}}$ and $f_{\text{rot}}^{\text{max}}$ limits, which can plausibly be attributed to P_{rot} . In those cases where multiple peaks are present, we generally adopted that with the highest amplitude (as discussed below, EPIC 210426551 and KIC 4857678 are two exceptions). The resulting photometric periods (P_{phot}) were then refined by fitting a sinusoidal function consisting of P_{phot} and its first four harmonics (see Sikora et al. 2019b). In Table 4 we report the derived P_{phot} values along with their 1σ uncertainties. We also report the equatorial velocities derived under the assumption that $P_{\text{phot}} = P_{\text{rot}}$ ($v_{\text{eq}}^{\text{phot}}$).

For 5 of the targets (EPIC 210355746, EPIC 210384590, EPIC 210505125, EPIC 220533366, and KIC 7732964), the identified f_{phot} ($1/P_{\text{phot}}$) values correspond to the maximum amplitude signals that appear in the full LS periodogram (i.e. below the Nyquist frequency). Furthermore, these f_{phot} values do not appear to be harmonics of lower frequencies and also exhibit a first harmonic. In these cases, it is very likely that P_{phot} is the rotation period. The 3 targets for which this correspondance between P_{phot} and P_{rot} is more ambiguous are discussed below.

For EPIC 210426551, the highest amplitude peak has a frequency of 5.776 d^{-1} , however, it is likely the first harmonic of the lower-amplitude peak appearing at 2.888 d^{-1} . This lower frequency falls slightly above $f_{\text{rot}}^{\text{min}}$ and we therefore adopt it as the f_{phot} value (i.e. that which is most likely to correspond to f_{rot}). For KIC 4857678, the highest amplitude peak has a frequency of 1.329 d^{-1} , which corresponds to the 0.75 d photometric period reported by Howell et al. (2016). This frequency falls below $f_{\text{rot}}^{\text{min}} = 1.598 \text{ d}^{-1}$ implying that it cannot correspond to f_{rot} . The complex peak distribution of KIC 4857678’s periodogram is characteristically similar to that observed for the pulsating γ Dor stars (e.g. Balona et al. 2011; Antoci et al. 2019). Furthermore, KIC 4857678 has a similar spectral type (early to mid F) to the γ Dor stars (e.g. Krisciunas et al. 1993). We conclude that the variability detected in the light curve is most likely pulsational in origin and do not report a P_{phot} value. Finally, for KIC 6150124 a large number of peaks are apparent within the f_{rot} limits and are thus consistent with the star’s rotation frequency, however, these signals cannot easily be disentangled from the increased power at $f \lesssim 1 \text{ d}^{-1}$ caused by granulation (Yu et al. 2018).

7 DISCUSSION

It has been suggested that the 8 targets (3 from the *Kepler* mission and 5 from the *K2* mission) that were included in this study are possible candidates of the FK Comae type stars based on their enhanced X-ray and UV emission and their apparent rapid rotation rates (Howell et al. 2016). As discussed below, we find that none of the 8 targets can be

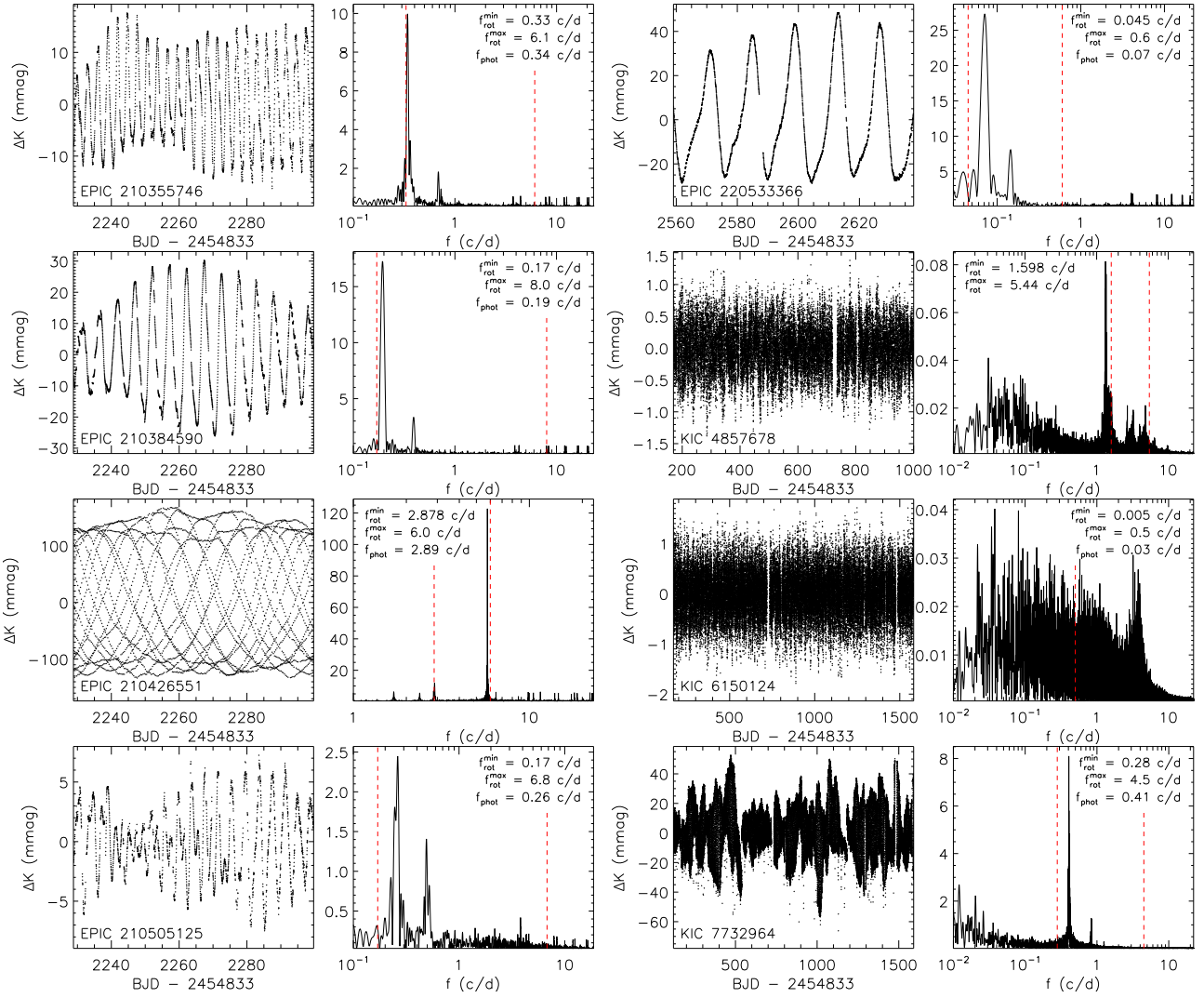


Figure 4. *Kepler* and *K2* light curves. The first and third columns show the full extracted and post-processed light curves; to the right of each light curves, we show the associated LS periodogram. For each of the periodograms, at least one peak is identified within the estimated lower and upper rotational frequency limits ($f_{\text{rot}}^{\text{min}}$ and $f_{\text{rot}}^{\text{max}}$, respectively), which are indicated by the red dashed lines. We note that these peaks may be associated with oscillation frequencies (e.g. KIC 6150124) or may correspond to integer multiples of f_{rot} . The photometric periods that can plausibly be attributed to each star’s rotation period ($P_{\text{phot}} = 1/f_{\text{phot}}$) are listed in Table 4.

considered FK Comae candidates based on the properties listed in Table 5.

The 3 *Kepler* targets that were observed in this study were also observed using a medium-resolution spectrograph by Howell et al. (2016), who reported that all of these stars exhibit $70 \lesssim v \sin i \lesssim 140 \text{ km s}^{-1}$. We derived $v \sin i$ values based on the newly obtained high-resolution spectra and found that, while these values are in agreement for KIC 4857678, our $v \sin i$ values are significantly lower for KIC 6150124 ($4 \pm 1 \text{ km s}^{-1}$ compared to a reported minimum value of $72.8 \pm 14.6 \text{ km s}^{-1}$) and KIC 7732964 ($23^{+1}_{-2} \text{ km s}^{-1}$ compared to a minimum value of $98.4 \pm 19.7 \text{ km s}^{-1}$). The discrepancies can likely be attributed to the fact that our observations have higher S/Ns ($\approx 200 - 600$ compared to $36 - 50$) and were obtained with a higher resolving power ($R \sim 65\,000$ compared to $R \sim 7\,700 - 10\,000$). Therefore, it is likely that both relatively high S/Ns ($\gtrsim 100$) and high-

resolution instruments are required in order to exclude false positives in the search for FK Comae type stars.

Out of the 8 targets included in our study, 5 are found to have $v \sin i$ values ranging from $9 - 23 \text{ km s}^{-1}$. The *Kepler* and *K2* light curves for these targets all reveal photometric variability that is consistent with rotational modulation. We derived rotational periods for these targets using the light curves, which, when combined with the stellar radii, yield equatorial velocities $\lesssim 30 \text{ km s}^{-1}$. The estimated rotation rates for these stars are considered anomalously high amongst evolved stars (e.g. Drake et al. 2002; Massarotti et al. 2008) but are not unusual amongst main sequence (MS) or pre-MS stars (e.g. Skumanich 1972; Hartmann et al. 1986; McQuillan et al. 2014). Three of the 5 stars in this $v \sin i$ range (EPIC 210505125, EPIC 210355746, and EPIC 210384590) lie along the MS, which is consistent with their derived $\log g$ values of ≈ 4.4 (cgs). EPIC 220533366 is a red giant branch (RGB) star with $v \sin i = 17 \pm 1 \text{ km s}^{-1}$;

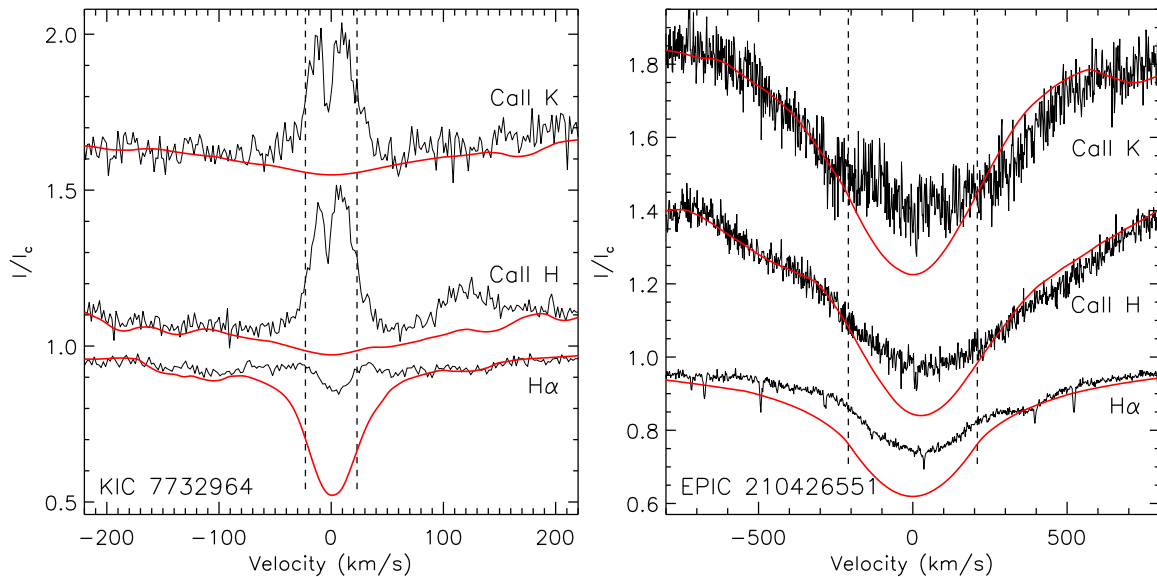


Figure 5. Observed spectra (black curves) compared with the synthetic models (red curves) generated using the best-fitting fundamental parameters (Table 2) for Ca II K, Ca II H, and H α . The vertical dashed lines correspond to each star’s $v \sin i$ values. *Left:* Clear, double-peaked emission is seen in all three lines for KIC 7732964. *Right:* For EPIC 210426551, we detect weak Ca II H and K emission. The apparent emission in H α is primarily inferred from the residuals between the observed and model profiles, however, it may be related to systematic errors in the normalization. In both cases, the detection of emission suggests that these stars are magnetically active.

however, we detected clear radial velocity variations and thus, we conclude that a plausible explanation for the high $v \sin i$ is that the star has been spun up by tidal interactions. For KIC 7732964 we derived a $v \sin i$ of $23^{+1}_{-2} \text{ km s}^{-1}$ and a v_{eq} of $30 \pm 2 \text{ km s}^{-1}$, which is very high considering that this star lies near the base of the RGB. Furthermore, as reported by Howell et al. (2016), it exhibits strong and complex H α and Ca II H and K emission (Fig. 5). Although KIC 7732964 shares similar characteristics with FK Com (albeit less extreme), it was observed only once in this study and therefore the presence of a binary companion cannot be ruled out.

The RGB star KIC 6150124 exhibits the lowest $v \sin i$ value ($4 \pm 1 \text{ km s}^{-1}$) within our sample. Along with the solar-type oscillations that are present in the *Kepler* light curve ($f \sim 3.5 \text{ cd}^{-1}$, Yu et al. 2018), we identified a possible rotational modulation signature corresponding to $P_{\text{rot}} = 31.3698 \pm 0.0001 \text{ d}$. The estimated P_{rot} and R values imply an unusually high equatorial velocity of $19.7 \pm 0.8 \text{ km s}^{-1}$; however, due to the increased low-frequency power produced by granulation, the estimated P_{rot} is not considered to be reliable. We conclude that this star is likely not a rapid rotator.

Two of the 8 targets in our study may be classified as ultra rapid rotators based on their extremely high $v \sin i$ values. For KIC 4857678, we derive a $v \sin i$ value of $111^{+6}_{-1} \text{ km s}^{-1}$ (≈ 34 per cent of v_{crit}) while no rotation period could be estimated from its *Kepler* light curve. For EPIC 210426551, we derive a $v \sin i$ value of $209 \pm 13 \text{ km s}^{-1}$ (≈ 68 per cent of v_{crit}) and a photometrically-inferred equatorial velocity of $184 \pm 12 \text{ km s}^{-1}$, which implies that the rotation axis has an inclination angle ~ 90 degrees. These two stars are discussed below.

KIC 4857678 has a fractional MS age of 0.7 estimated using evolutionary models (Ekström et al. 2012; Georgy et al. 2013). No Zeeman signatures were detected in the LSD

profiles (we obtained a minimum precision of $\sigma_{(B_z)} = 64 \text{ G}$) and no H α or Ca II H and K emission was detected suggesting that the star is not magnetically active. The transition between those MS stars with deep convective envelopes and those with shallow convective envelopes is predicted to occur near $\approx 1.4 M_{\odot}$ (e.g. van Saders & Pinsonneault 2012; Cantiello & Braithwaite 2019); this boundary approximately coincides with the gradual increase in frequency of strongly magnetic A-type (Ap) stars (e.g. Fig. 17 of Sikora et al. 2019a), which account for $\lesssim 10$ per cent of all MS A-type stars. Based on KIC 4857678’s derived mass of $1.29^{+0.05}_{-0.07} M_{\odot}$, it is plausible that its convective envelope is shallow and unable to generate magnetic fields that might otherwise enable significant spin-down via magnetic braking to take place. The fact that we do not detect any spectroscopic evidence of magnetic activity appears to conflict with the strong X-ray and UV emission that was detected for this star (Smith et al. 2015). No evidence of a short-period binary companion was found based on the 2 observations that were obtained. Due to the relatively low angular resolution of the X-ray and UV instruments, the detected emission may be associated with a widely separated magnetically active companion (e.g. a late M-type star) or a hot white dwarf (e.g. Heise 1985). Ultimately, we conclude that this star’s apparent rapid rotation rate is likely consistent with the current predictions of single star evolution.

As with KIC 4857678, we did not detect Zeeman signatures for EPIC 210426551 although this may be due to the large uncertainties ($\sigma_{(B_z)} = 335 \text{ G}$) that were obtained primarily as a result of the star’s high $v \sin i$ value. Comparisons between the observed spectra and the model spectra generated using the best-fitting parameters do yield possible evidence of magnetic activity via weak Ca II H and K emission and possibly weak H α emission (Fig. 5). Several examples of young, magnetically active solar-type stars with

Table 5. The defining properties of known FK Comae stars (FK Com, ET Dra, and HD 199178) compared with those of the 8 stars in our sample. Columns 2 and 3 specify whether the star has evolved off of the MS or if it has a short-period companion. Columns 4 and 5 specify whether X-ray emission or optical emission (Ca II K, Ca II H, and/or H α) has been detected. Columns 6 and 7 list each star’s $v \sin i$ value and estimated mass.

ID	Post-MS	Short- P_{orb} Comp.	X-ray Em.	Optical Em.	$v \sin i$ (km s $^{-1}$)	M (M_{\odot})
FK Com	Yes	No	Yes	Yes	160 ^a	2.2 ^b
ET Dra	Yes	No	Yes	Yes	30-40 ^c	$\approx 1.4^{\dagger}$
HD 199178	Yes	No	Yes	Yes	80 ^d	2.2 ^b
EPIC 210355746	No	No	Yes	Yes	21	0.97
EPIC 210384590	No	?	Yes	Yes	9	0.86
EPIC 210426551	No	?	Yes	Yes	209	1.05
EPIC 210505125	No	Yes	Yes	No	11.7/12.8	1.04
EPIC 220533366	Yes	Yes	Yes	Yes	17	1.2
KIC 4857678	No	No	Yes	No	111	1.29
KIC 6150124	Yes	?	Yes	No	4	2.2
KIC 7732964	Yes	?	Yes	Yes	23	0.77

^a Huenemoerder et al. (1993), ^b Gondoin (1999), ^c Silva et al. (1985),

^d Huenemoerder (1986), [†] Estimated using *Gaia* DR2 T_{eff} and L values and solar-metallicity Ekström et al. (2012) evolutionary models.

$v \sin i$ values $> 200 \text{ km s}^{-1}$ have been previously reported (e.g. Marsden et al. 2009). Under the assumption that magnetic activity ought to increase with increasing rotational velocity, one might expect spin-down to occur more rapidly in these cases, thereby preventing such rapid rotators from appearing near the end of the pre-MS phase. It has been proposed that these observations may be explained by the fact that the efficiency of magnetic braking does not continue to increase with increasing rotational velocity above a certain saturation limit (e.g. Vilhu 1984; Krishnamurthi et al. 1997; Wright et al. 2011). Models of the rotational evolution of solar-type stars that incorporate a saturation threshold have successfully replicated the observed convergence towards low rotational velocities ($\lesssim 10 \text{ km s}^{-1}$) that occurs after $\sim 1 \text{ Gyr}$ (e.g. Spada et al. 2011; Amard et al. 2016).

Based on the preceding discussion, it may only be possible to explain EPIC 210426551’s extremely high rotational velocity as the product of a single star evolutionary history if it is very young (i.e. either a ZAMS or pre-MS star). For EPIC 210426551, we derive a metallicity of $[M/H] = -0.4 \pm 0.1$, which permits two possibilities in terms of its evolutionary state: either it is close to the terminal-age MS (TAMS) (see Fig. 3) or it is a pre-MS star approaching the ZAMS. Comparisons between the *Gaia* DR2 astrometry, proper motion, and distance measurements with those of nearby open clusters (Kharchenko et al. 2013) did not yield any clear potential memberships that could have otherwise been used to infer age constraints. One possible indication of youth is the detection of excess IR flux, which is generally indicative of dust particles (e.g. Wyatt 2008). Using the criterion proposed by Wu et al. (2013) based on 2MASS and WISE photometry (Cohen et al. 2003; Wright et al. 2010), we find no indication of an IR excess for EPIC 210426551.

We note that if the derived metallicity for EPIC 210426551 is inaccurate and it instead has a solar metallicity, then it is expected to have a similar age and mass to KIC 4857678. In this scenario, the star’s high rotation rate can be explained either by the fact that (1)

the star is not subject to significant magnetic braking due to a shallow or non-existent convective envelope (similar to the scenario proposed for KIC 4857678) or (2) that the star is very young (either ZAMS or pre-MS). Considering that we have detected evidence of magnetic activity (as noted above; see Fig. 5), it appears most likely that if EPIC 210426551 has a solar metallicity, the latter of these two explanations is more plausible. Of course, only a single observation was obtained in this study and we cannot yet rule out the possibility that this star has been spun-up by binary interactions (N.B. the ‘duplicated_source’ flag in the *Gaia* DR2 catalogue is ‘false’ implying that no additional sources associated with EPIC 210426551 were detected). Therefore, without having better constraints on either this object’s age or whether it has a short-period binary companion, we conclude that the explanation for EPIC 210426551’s high rotational velocity as being the product of a stellar merger event remains viable.

Stellar merger events are predicted to occur largely as a result of primordial binary evolution (e.g. Webbink 1976; Politano et al. 2010; Howitt et al. 2020). Theoretical predictions related to this formation channel have suggested that the merging of the two stars may be facilitated by the presence of a widely separated third component via Kozai-Lidov cycles (Kozai 1962; Lidov 1962; Portegies Zwart & van den Heuvel 2016; Izzard et al. 2018). It is therefore interesting to note that, in the case of the 2 targets identified here as potential stellar merger candidates (KIC 7732964 and EPIC 210426551), high-resolution speckle interferometric measurements have yielded detections of wide binary companions ($P_{\text{orb}} \gtrsim 17 \text{ yrs}$) (Howell et al., in prep.). Such detections, if shown to be related to stellar mergers, may provide a further identifying criterion in addition to those previously discussed (e.g. rapidly rotating, magnetically active evolved stars).

8 SUMMARY

We have obtained 1-2 high-resolution spectropolarimetric (Stokes V) observations for a small subset (8 targets) of a larger sample of candidate FK Comae type stars that were first identified by [Smith et al. \(2015\)](#) and [Howell et al. \(2016\)](#). We conclude that none of the 8 targets are FK Comae candidates based on (1) the detection of binary companions, (2) their inferred evolutionary states, or (3) low rotational velocities ($< 10 \text{ km s}^{-1}$) inferred from spectroscopically-derived $v \sin i$ values and/or photometrically-inferred rotation periods. This is not particularly surprising considering the extreme rarity of FK Comae type stars. However, 2 targets included in our study (KIC 7732964 and EPIC 210426551) are found to exhibit characteristics that are consistent with some of the predicted properties of stellar merger products (i.e. the leading explanation for FK Com's unusual characteristics) and, based on the currently available observations, they cannot be ruled out as such. At a minimum, additional spectra are required for these 2 targets in order to search for binary companions that may explain their anomalously high rotational velocities. If no short-period binary companions are found to be associated with these stars, obtaining better constraints on (1) their apparent magnetic activity using instruments such as ESPaDOnS@CFHT or SPIRou@CFHT or on (2) the presence of cool dust using instruments provided for example by SOFIA, may yield important clues about the nature of these objects and stellar merger products in general.

ACKNOWLEDGMENTS

GAW acknowledges support in the form of a Discovery Grant from the Natural Science and Engineering Research Council (NSERC) of Canada.

REFERENCES

- Amard L., Palacios A., Charbonnel C., Gallet F., Bouvier J., 2016, *A&A*, 587, A105
- Andrae R., et al., 2018, *A&A*, 616, A8
- Antoci V., et al., 2019, arXiv:1909.12018 [astro-ph]
- Asplund M., Grevesse N., Sauval A. J., Scott P., 2009, *ARA&A*, 47, 481
- Ayres T. R., et al., 2016, *ApJS*, 223, 5
- Bailer-Jones C. A. L., Rybizki J., Foesneau M., Mantelet G., Andrae R., 2018, *AJ*, 156, 58
- Balona L. A., Guzik J. A., Uytterhoeven K., Smith J. C., Tenenbaum P., Twicken J. D., 2011, *Monthly Notices of the Royal Astronomical Society*, 415, 3531
- Bopp B. W., Rucinski S. M., 1981, in Sugimoto D., Lamb D. Q., Schramm D. N., eds, IAU Symposium Vol. 93, Fundamental Problems in the Theory of Stellar Evolution. p. 177
- Bouvier J., Forestini M., Allain S., 1997, *Astronomy and Astrophysics*, 326, 1023
- Brown T. M., Latham D. W., Everett M. E., Esquerdo G. A., 2011, *AJ*, 142, 112
- Cannon A. J., Pickering E. C., 1993, *VizieR Online Data Catalog*, p. III/135A
- Cantiello M., Braithwaite J., 2019, arXiv:1904.02161 [astro-ph]
- Carlberg J. K., Majewski S. R., Patterson R. J., Bizyaev D., Smith V. V., Cunha K., 2011, *ApJ*, 732, 39
- Casagrande L., Schönrich R., Asplund M., Cassisi S., Ramírez I., Meléndez J., Bensby T., Feltzing S., 2011, *A&A*, 530, A138
- Castelli F., Kurucz R. L., 2003, in Proceedings of the 210th Symposium of the IAU. Publications of the Astronomical Society of the Pacific, Uppsala University, Uppsala, Sweden, p. A20 (arXiv:astro-ph/0405087)
- Cohen M., Wheaton W. A., Megeath S. T., 2003, *AJ*, 126, 1090
- Cutispoto G., Pastori L., Pasquini L., de Medeiros J. R., Tagliaferri G., Andersen J., 2002, *A&A*, 384, 491
- Donati J.-F., Semel M., Carter B. D., Rees D. E., Cameron A. C., 1997, *MNRAS*, 291, 658
- Drake N. A., de la Reza R., da Silva L., Lambert D. L., 2002, *The Astronomical Journal*, 123, 2703
- ESA 1997, The HIPPARCOS and TYCHO Catalogues. Astrometric and Photometric Star Catalogues Derived from the ESA HIPPARCOS Space Astrometry Mission. ESA Special Publication Vol. 1200, Noordwijk, Netherlands: ESA Publications Division
- Ekström S., et al., 2012, *A&A*, 537, A146
- Fekel F. C., Balachandran S., 1993, *The Astrophysical Journal*, 403, 708
- Frasca A., et al., 2016, *A&A*, 594, A39
- Gaia Collaboration et al., 2018, *A&A*, 616, A1
- Garrison R., 1984, The MK Process and Stellar Classification: Proceedings of the Workshop in Honor of W.W. Morgan and P.C. Keenan Held at the University of Toronto, Canada, June 1983. Dunlop observatory. University of Toronto
- Gehrels N., et al., 2004, *The Astrophysical Journal*, 611, 1005
- Georgy C., et al., 2013, *A&A*, 558, A103
- Gondoin P., 1999, *Astronomy and Astrophysics*, 352, 217
- Gontcharov G. A., Mosenkov A. V., 2017, *MNRAS*, 472, 3805
- Gray D. F., 2005, *The Observation and Analysis of Stellar Photospheres*, third edn. Cambridge University Press, doi:10.1017/CBO9781316036570
- Hartmann L., Hewett R., Stahler S., Mathieu R. D., 1986, *ApJ*, 309, 275
- Hauck B., Mermilliod M., 1998, *A&AS*, 129, 431
- Heise J., 1985, *Space Science Reviews*, 40, 79
- Herbig G. H., 1958, *ApJ*, 128, 259
- Howell S. B., et al., 2014, *PASP*, 126, 398
- Howell S. B., Mason E., Boyd P., Smith K. L., Gelino D. M., 2016, *ApJ*, 831, 27
- Howitt G., Stevenson S., Vigna-Gómez A., Justham S., Ivanova N., Woods T. E., Neijssel C. J., Mandel I., 2020, *Monthly Notices of the Royal Astronomical Society*, 492, 3229
- Huenemoerder D. P., 1986, *The Astronomical Journal*, 92, 673
- Huenemoerder D. P., Ramsey L. W., Buzasi D. L., Nations H. L., 1993, *The Astrophysical Journal*, 404, 316
- Izzard R. G., Preece H., Jofre P., Halabi G. M., Masseron T., Tout C. A., 2018, *Monthly Notices of the Royal Astronomical Society*, 473, 2984
- Jetsu L., Huovelin J., Savanov I., Tuominen I., 1991, *Astronomy & Astrophysics*, 248, 574
- Keenan P. C., Morgan W. W., 1941, *The Astrophysical Journal*, 94, 501
- Kharchenko N. V., Piskunov A. E., Schilbach E., Röser S., Scholz R.-D., 2013, *A&A*, 558, A53
- Kochukhov O., Makaganiuk V., Piskunov N., 2010, *A&A*, 524, A5
- Korhonen H., Hubrig S., Berdyugina S. V., Granzer T., Hackman T., Schöller M., Strassmeier K. G., Weber M., 2009, *Monthly Notices of the Royal Astronomical Society*, 395, 282
- Kozai Y., 1962, *The Astronomical Journal*, 67, 591
- Krisciunas K., et al., 1993, *Monthly Notices of the Royal Astronomical Society*, 263, 781
- Krishnamurthi A., Pinsonneault M. H., Barnes S., Sofia S., 1997, *ApJ*, 480, 303
- Lidov M. L., 1962, *Planetary and Space Science*, 9, 719

- Lomb N. R., 1976, *Ap&SS*, 39, 447
- Maeder A., Meynet G., 2000, *Astronomy and Astrophysics*, 361, 159
- Marsden S. C., Carter B. D., Donati J.-F., 2009, *Monthly Notices of the Royal Astronomical Society*, 399, 888
- Massarotti A., Latham D. W., Stefanik R. P., Fogel J., 2008, *The Astronomical Journal*, 135, 209
- McQuillan A., Mazeh T., Aigrain S., 2014, *ApJS*, 211, 24
- Molenda-Zakowicz J., Jerzykiewicz M., Frasca A., Catanzaro G., Kopacki G., Latham D. W., 2010, arXiv:1005.0985 [astro-ph]
- Mowlavi N., Eggenberger P., Meynet G., Ekström S., Georgy C., Maeder A., Charbonnel C., Eyer L., 2012, *A&A*, 541, A41
- Oliveira J. M., Foing B. H., 1999, *Astronomy and Astrophysics*, 343, 213
- Politano M., van der Sluys M., Taam R. E., Willems B., 2010, *ApJ*, 720, 1752
- Portegies Zwart S. F., van den Heuvel E. P. J., 2016, *Mon. Not. R. Astron. Soc.*, 456, 3401
- Privitera G., Meynet G., Eggenberger P., Vidotto A. A., Villaver E., Bianda M., 2016, *A&A*, 591, A45
- Ramsey L. W., Nations H. L., Barden S. C., 1981, *The Astrophysical Journal*, 251, L101
- Ryabchikova T., Piskunov N., Kurucz R. L., Stempels H. C., Heiter U., Pakhomov Y., Barklem P. S., 2015, *Physica Scripta*, 90, 054005
- Scargle J. D., 1982, *ApJ*, 263, 835
- Shultz M. E., Wade G. A., Rivinius T., Alecian E., Neiner C., Petit V., Wisniewski J. P., 2019, *MNRAS*, 485, 1508
- Shulyak D., Tsymbal V., Ryabchikova T., Stütz C., Weiss W. W., 2004, *A&A*, 428, 993
- Sikora J., Wade G. A., Power J., Neiner C., 2019a, *MNRAS*, 483, 2300
- Sikora J., et al., 2019b, *MNRAS*, 487, 4695
- Silva D. R., Liebert J., Stocke J. T., Aaronson M., 1985, *PASP*, 97, 1096
- Simon T., Drake S. A., 1989, *ApJ*, 346, 303
- Simón-Díaz S., Herrero A., Esteban C., Najarro F., 2006, *A&A*, 448, 351
- Skumanich A., 1972, *The Astrophysical Journal*, 171, 565
- Smith J. C., et al., 2012, *PASP*, 124, 1000
- Smith K. L., et al., 2015, *AJ*, 150, 126
- Spada F., Lanzafame A. C., Lanza A. F., Messina S., Collier Cameron A., 2011, *Monthly Notices of the Royal Astronomical Society*, pp no–no
- Strassmeier K. G., Bartus J., Ko Z., 1998, *Astronomy and Astrophysics*, 336, 587
- Tkachenko A., 2015, *A&A*, 581, A129
- Vilhu O., 1984, *Astronomy and Astrophysics*, 133, 117
- Wade G. A., Donati J.-F., Landstreet J. D., Shorlin S. L. S., 2000, *MNRAS*, 313, 851
- Webbink R. F., 1976, *The Astrophysical Journal*, 209, 829
- Wright E. L., et al., 2010, *The Astronomical Journal*, 140, 1868
- Wright N. J., Drake J. J., Mamajek E. E., Henry G. W., 2011, *ApJ*, 743, 48
- Wu C.-J., Wu H., Lam M.-I., Yang M., Wen X.-Q., Li S., Zhang T.-J., Gao L., 2013, *ApJS*, 208, 29
- Wyatt M. C., 2008, *Annual Review of Astronomy and Astrophysics*, 46, 339
- Yu J., Huber D., Bedding T. R., Stello D., Hon M., Murphy S. J., Khanna S., 2018, *ApJS*, 236, 42
- da Silva R. R., Canto Martins B. L., De Medeiros J. R., 2015, *ApJ*, 801, 54
- de Medeiros J. R., Da Rocha C., Mayor M., 1996, *Astronomy and Astrophysics*, 314, 499
- van Saders J. L., Pinsonneault M. H., 2012, *ApJ*, 746, 16

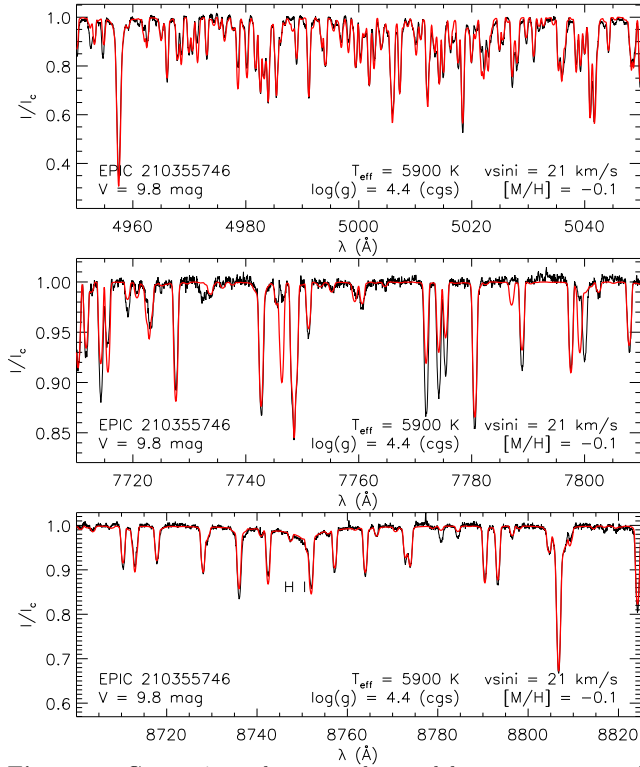


Figure 6. Comparisons between the model spectra generated using the best-fitting parameters (red curve) and the observed spectra (black curve) for the 3 selected spectral windows (4950 – 5050 Å, 7710 – 7810 Å, and 8700 – 8825 Å).

APPENDIX

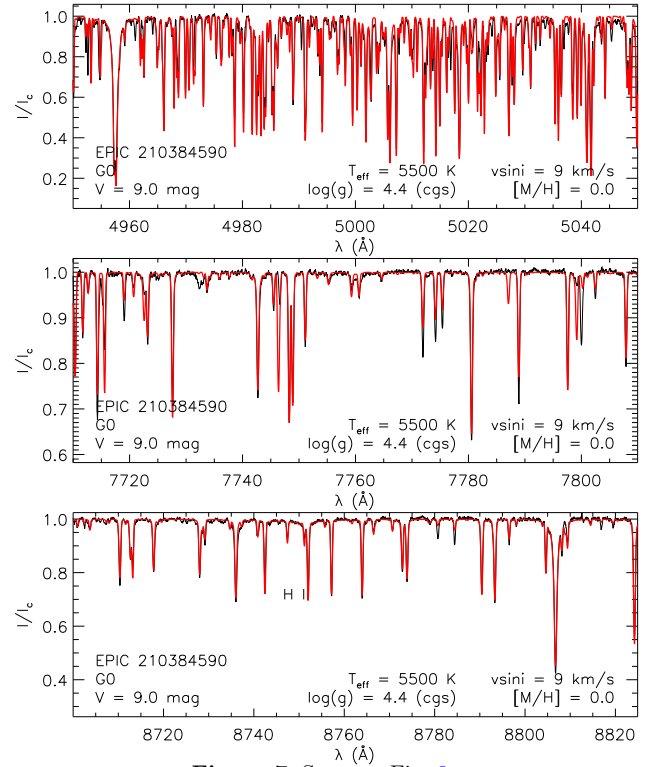


Figure 7. Same as Fig. 6.

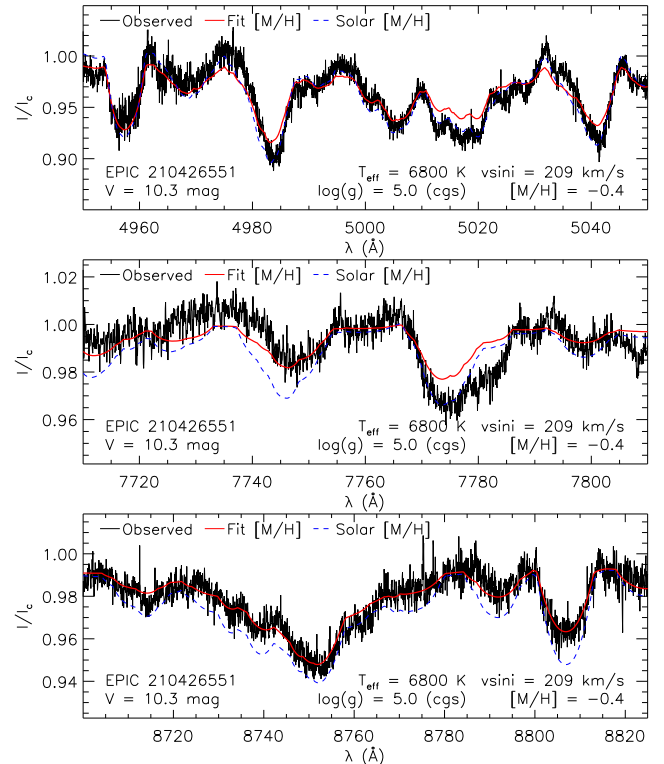


Figure 8. Same as Fig. 6. The dashed blue curve corresponds to the model spectra generated using the best-fitting parameters but with a solar metallicity ($[M/H]=0$).

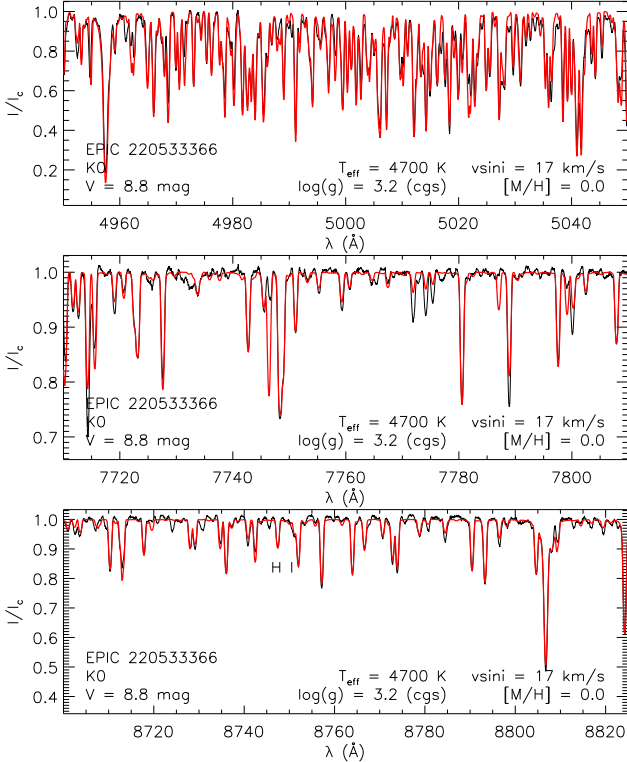


Figure 9. Same as Fig. 6.

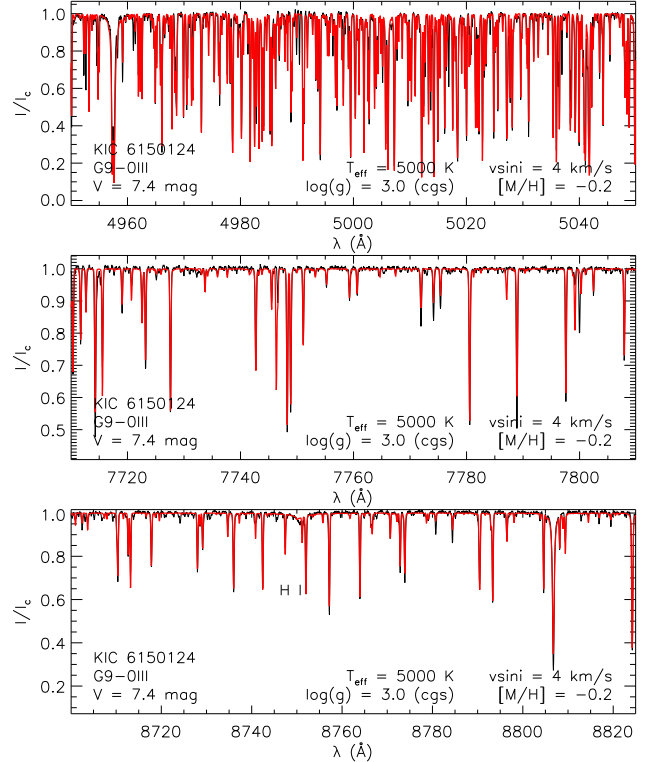


Figure 11. Same as Fig. 6.

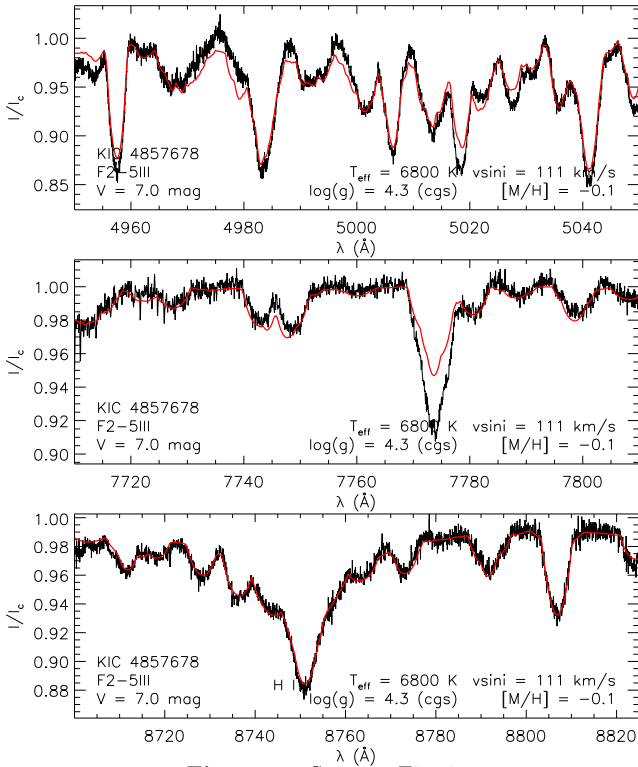


Figure 10. Same as Fig. 6.

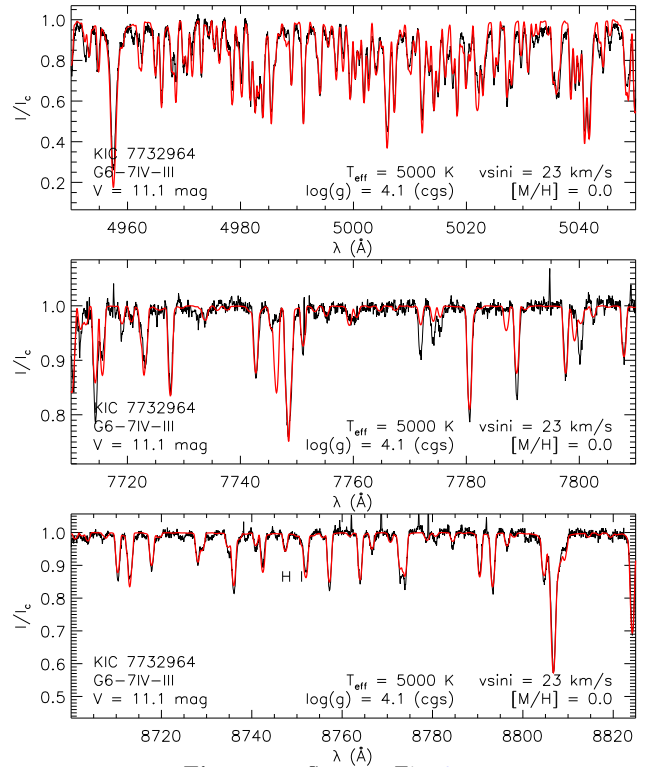


Figure 12. Same as Fig. 6.